GEOPHYSICS

Rapid fault healing from cementation controls the dynamics of deep slow slip and tremor

Amanda M. Thomas[1]*†, James M. Watkins[1]†, Nicholas Beeler[2], Melodie E. French[3], Whitney M. Behr[4], Mark H. Reed[5]

Despite its status as one of the most important discoveries in geophysics, the physical mechanism(s) responsible for slow slip events (SSEs) are not well understood. Here, we synthesize observations of deep SSEs in the Cascadia Subduction Zone and argue that rapid, cohesive fault strengthening may control the dynamics of deep SSEs. Cohesive strength is frequently ignored in constitutive laws used to describe fault rheology in numerical simulations of earthquakes and SSEs alike. To demonstrate its importance, we perform and analyze a suite of petrological experiments that simulate fault healing under representative pressure and temperature conditions. We show that significant cohesive strength recovery caused by dissolution-precipitation processes occurs on timescales of just a few hours. Together, our experimental and observational results support the idea that cohesion is a key component of fault strength under SSE conditions and highlight the need for its inclusion in both future experiments and numerical models of fault slip.

INTRODUCTION

Faults globally accommodate tectonic loading at different slip speeds controlled by differing fault mechanical properties. Slow slip events (SSEs) are a type of slow, transient fault slip during which the slip rate accelerates to speeds that are only one or two orders of magnitude faster than the background tectonic loading rate [e.g., (*1*, *2*)]. SSEs occur in subduction zones around the world and, unlike traditional earthquakes, generate weak or no discernable seismic waves. High-quality, densely spaced seismic networks, such as the one on Southern Vancouver Island in the Cascadia Subduction Zone (Fig. 1A), are required to observe the rich seismic manifestation of slow earthquakes. During SSEs in Cascadia, recorded seismograms become enriched in frequencies between 1 and 10 Hz (Fig. 1B) (*3*, *4*). Data mining techniques applied to these anomalous seismograms identify low-frequency earthquakes (LFEs; Fig. 1C), defined as earthquakes that are depleted in high-frequency content and have longer durations than shallow earthquakes of similar magnitude (*5*, *6*). When superimposed in time, LFEs make up the tectonic tremor signal that commonly accompanies SSEs (*5*). LFEs can be grouped into families on the basis of waveform similarity; each instance of an LFE within a family reflects slip at the same or nearly the same location (*5*, *7*). LFEs likely reflect largely aseismic fault slip and provide a unique opportunity to study the spatial and temporal evolution of slip during SSEs (*8*).

Secondary slip fronts

Analysis of the space and time progression of LFEs during SSEs suggests that SSEs in Cascadia contain many smaller-scale, secondary slip fronts that can propagate in a variety of directions, on a variety of length and timescales [e.g., (*9*–*14*)]. For example, Fig. 2A shows the space and time progression of LFEs during a large SSE that occurred in September 2012 beneath Southern Vancouver Island (Fig. 1A). Each LFE family occupies a constant y position (i.e., distance along strike), and each occurrence of that LFE is indicated by a dot color coded by magnitude. The main SSE front first manifests in the north (40 km) around 6 September and propagates southward over 80 km along strike in 11 days or ~10 km/day. Within a given LFE family (e.g., family 141 shown in Fig. 2B), the event rate is generally high early in the SSE (the first few hours) and decreases as the SSE progresses (*11*). However, this decrease is not uniform—it contains many LFEs occurring in rapid succession punctuated by quiescent periods that can last one or more days before additional LFEs occur (Fig. 2B) (*7*, *11*). This later LFE activity has the largest LFE-derived moment rates of the entire SSE (Fig. 2A) (*7*). Given that LFEs are thought to reflect surrounding fault slip, these bursts represent slip distinct from the main front. They also progress coherently in space beginning near the main front, migrating back along strike (e.g., Fig. 2C) and activating the same LFE families that recently slipped in the main SSE front (*7*). Similar observations have been reported in Japan (*15*, *16*), Mexico (*17*), and Parkfield, US (*18*), suggesting that secondary fronts are a ubiquitous feature of deep slow slip.

The largest and most distinct secondary fronts—referred to as rapid tremor reversals by Houston *et al.* (*10*)—are observed in both tremor and LFE datasets (Fig. 2A). These fronts typically initiate within 1 to 10 km of the main front, propagate 10 to 40 times faster, and span durations of 2 to 6 hours. They rerupture fault segments that hosted LFEs in the preceding days (Fig. 2C) (*11*). Measurements of surface strain indicate that these events have average magnitudes of M_w (moment magnitude) ~ 5.1, whereas the daily moment release in large SSEs is equivalent to a $M_w = 5.6$ (*19*). The large secondary fronts release a median of 8 kPa of shear stress, ~50% of the stress drop of typical large-magnitude SSEs in Cascadia (*19*). It is worth noting that there is significant scatter on these estimates, with most secondary fronts releasing 10 to 100% of the stress drop in the SSE, but they remain the best available. They are also broadly consistent with the LFE-derived moment release in individual families. For example, family 141 shown in Fig. 2B accommodates only about 40% of the cumulative moment release in the main front before

---

[1]Department of Earth and Planetary Sciences, University of California, Davis, Davis, CA, USA. [2]U.S. Geological Survey Cascades Observatory, Vancouver, WA, USA. [3]Department of Earth Sciences, Rice University, Houston, TX, USA. [4]Department of Earth Sciences, ETH Zürich, Zürich, Switzerland. [5]Department of Earth Sciences, University of Oregon, Eugene, OR, USA.
*Corresponding author. Email: amthom@ucdavis.edu
†These authors contributed equally to this work.

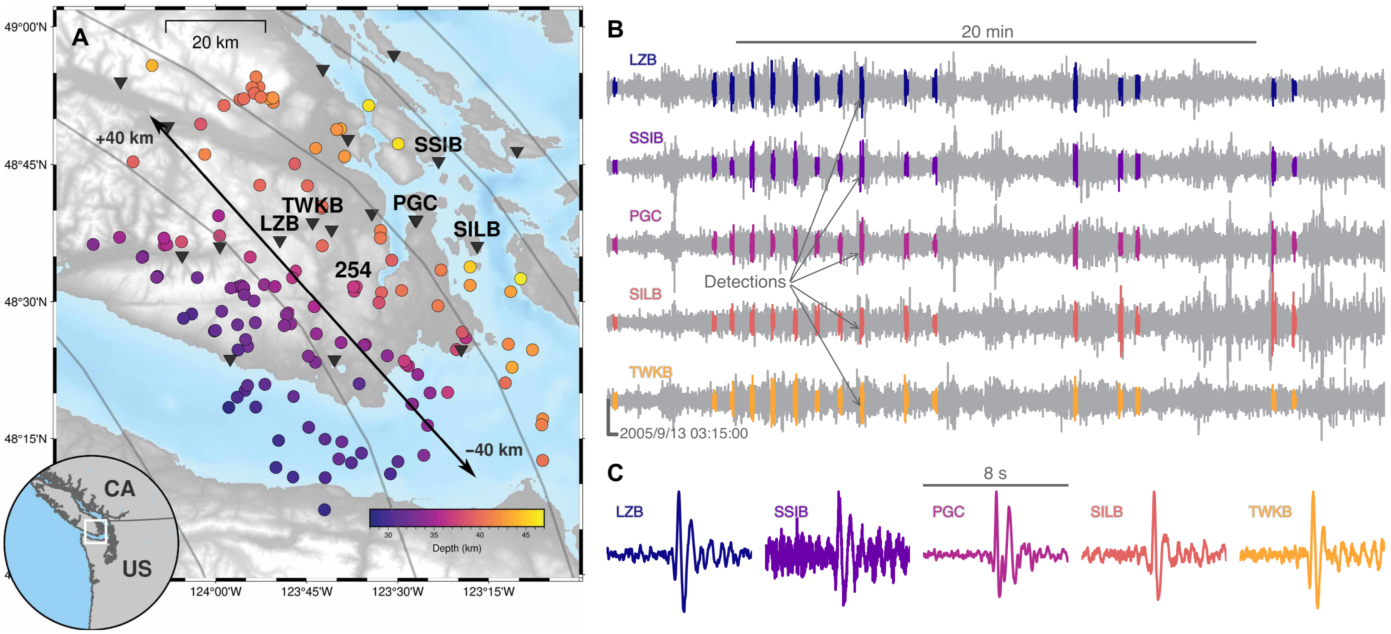

Fig. 1. Southern Vancouver Island LFE locations and waveforms. (**A**) Map of southern Vancouver Island LFEs from Bostock *et al.* (*7*). LFE locations are indicated by circles color coded by depth. Stations used in the Bostock *et al.* (*7*) study are shown as triangles. Stations used in (B) are annotated with station names. The inset shows global context. (**B**) Twenty minutes of high-frequency waveforms recorded at annotated stations shown in (A). Each detection of LFE family 254 in this time window is color coded by station. (**C**) LFE waveforms with 8-s durations recorded at stations annotated in (A).

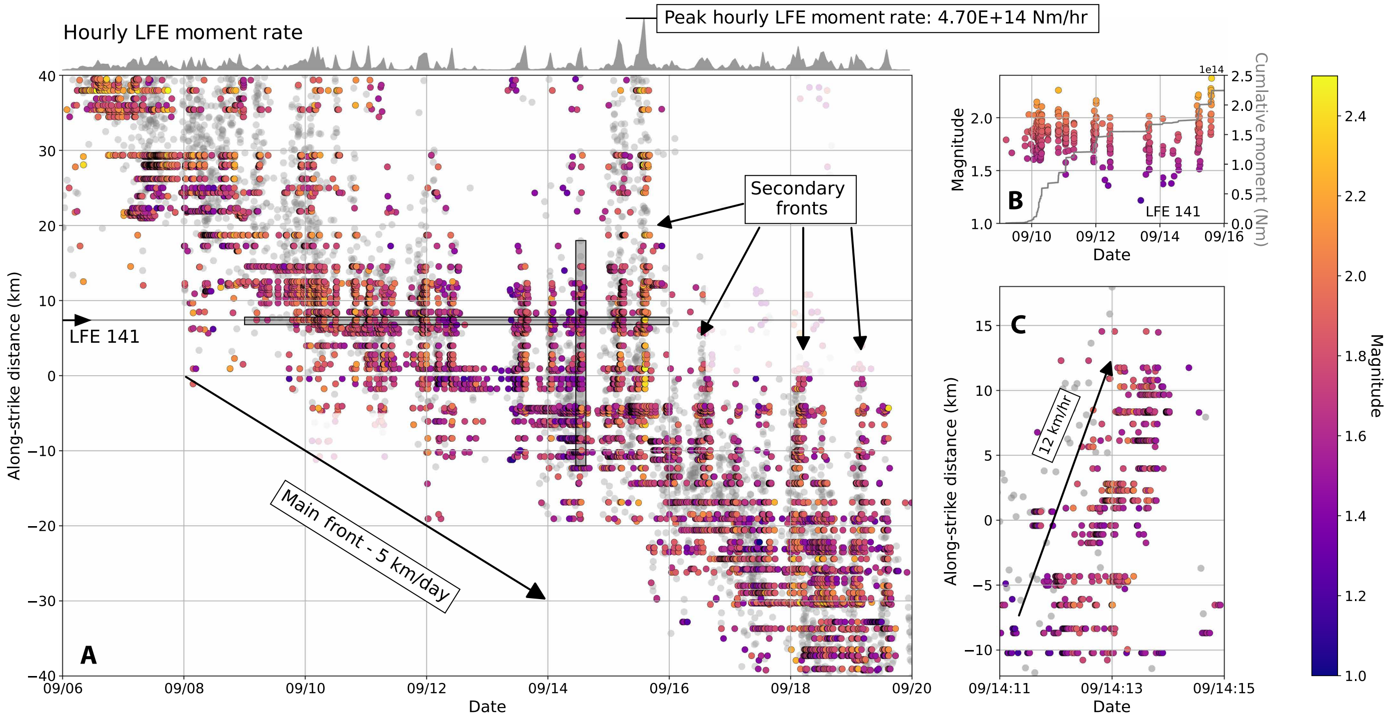

Fig. 2. Spatial and temporal evolution of the 2012 SSE. (**A**) LFEs from the Bostock *et al.* (*7*) catalog are plotted as a function of date and along-strike distance (Fig. 1A) color coded by magnitude. Gray circles indicate tremor locations from the catalog of Wech and Creager (*3*). The main front propagates southward at ~5 km/day, and secondary fronts manifest as vertically oriented groups of events closely spaced in time (four are marked with arrows). The direction of propagation of the main front and the along-strike location of LFE 141 are marked. The horizontal and vertical gray boxes outline the regions shown in (B) and (C), respectively. hr, hour. (**B**) LFEs in family 141 plotted as a function of time and magnitude. The gray line shows cumulative moment in newton-meters. (**C**) Zoom-in of the region outlined by the yellow box in (A) showing a secondary front illuminated by both LFEs and tremor on 14 September that propagates at a speed of ~12 km/hour.

12 September. The remaining 60% of moment release occurs in six secondary fronts that occur between 12 September and 16 September.

Tidal stresses and elevated pore fluid pressure

Several studies have shown that LFEs are sensitive to small-magnitude tidal stresses (*5*, *20*–*24*). In Cascadia, increases in slip-encouraging shear stress of only ~2 kPa in magnitude (*13*, *23*) result in increased LFE or tremor rates. LFEs are far less sensitive to tidal normal stress variations that are significantly larger than tidally induced shear stress variations (*13*, *25*). Sensitivity to tidal shear stress is not constant throughout the SSE. The early LFEs that occur as part of the main front are not significantly influenced by the tides. Later in the SSE, the less-frequent, larger-scale discrete bursts of LFEs that signal secondary fronts, like those shown in Fig. 2C, correlate with tides and are almost always tidally triggered [e.g., (*12*, *13*, *23*, *26*)].

Multiple lines of evidence indicate that pressurized pore fluids are present in the SSE source region and likely are required for slow slip to occur. First, seismic imaging constraints reveal that elevated Poisson ratios are pervasive in the SSE source region [e.g., (*27*–*32*)]. Second, the observed sensitivity of LFEs and tremor to small-magnitude tidal shear stress changes resolved on the fault is most easily explained by appealing to nearly lithostatic pore fluid pressures [e.g., (*13*, *21*, *22*, *25*, *33*)]. Third, analysis of exhumed subduction complexes thought to reflect deformation mechanisms and conditions present in SSE environs shows pervasive evidence for fluids in the form of veins (*2*, *34*, *35*). Last, analysis of the thermal and petrologic environment in warm subduction zones that host SSEs reveals that the presence of fluids is expected (*36*). At ~500°C and confining pressures near 1 GPa, pressurized fluids introduced via prograde metamorphic dehydration reactions and retained by low-porosity and low-permeability fabrics are expected [e.g., (*32*, *37*, *38*)].

Cementation/cohesion and secondary fronts

The occurrence of large-scale secondary fronts is enigmatic. Assuming that both SSE and secondary fronts occur on the same fault surface and that SSEs arise from frictional slip [e.g., (*33*)], shear stress on the fault should increase until it exceeds the fault strength and frictional sliding commences (*39*). Secondary fronts occur hours after the passage of the main front, slipping the same section of fault, and relieve a significant fraction (i.e., ~50%) of the stress released in the main front. This raises the question as to why, if the fault has additional stress to relieve, it is not accommodated during the main SSE front. The observations of tidal triggering described in the previous section indicate that tidal stresses play a key role in the generation of the late occurring secondary fronts by reloading the fault on short (i.e., hourly) timescales. We note that in some cases, changes in tidal shear stresses of ~2 kPa cannot supply the entire stress drop (8 kPa on average) for the secondary fronts. So, either continued stress transfer from the main front [e.g., (*16*)], a reduction of fault strength owing to migrating pore fluid pressure pulses [e.g., (*40*)], or some other mechanism must also contribute.

Applying shear stress to a fault with no strength will simply cause the fault to creep. Generating slip fronts like those observed requires a corresponding increase in fault strength on similarly short timescales. Rate-and-state friction is often invoked in numerical models of SSEs and describes how the slip rate and conditions on the fault surface influence the frictional resistance experienced during slip. In this framework, fault strengthening results from time-dependent increases in fault contact area as a result of creep at asperity contacts and/or time-dependent increases in the strength of asperity contacts (*41*). Secondary fronts arise frequently in simulations that incorporate tidal loading on a fault obeying rate-and-state friction, but the modeled fronts are not representative of actual secondary fronts because they do not repeatedly rupture the same section of fault and because the simulated fronts have slower propagation speeds than the observed fronts. Matching the observed propagation speeds requires stress drops that are comparable to those of the main front (*11*, *16*, *42*); hence, a source of additional fault strength is needed. Follow-up studies have explored the role of heterogeneity and fluids in producing secondary fronts with some success (*40*, *43*), but it is unclear how tuned the parameters must be to reproduce representative fronts.

Observations of natural faults, including those exhumed from conditions similar to modern deep SSE environs, indicate that fluid mass transport may strongly influence fault properties (*34*, *44*–*49*). Mineral cements and vein fill, typically composed primarily of quartz, are frequently observed on natural faults, including those exhumed from both seismogenic depths and from conditions similar to modern deep SSE environs [e.g., (*2*, *34*, *35*, *48*, *50*)], suggesting that cementation, or precipitation of a binding material dissolved in the pore fluid, plays an important role in fault deformation processes.

During SSEs, we envisage the fracture of asperity contacts, redistribution of stresses, and increased connectivity of fluid-filled pore spaces. Once slip ceases, the fault surface contains numerous strong asperity contacts that behave frictionally. At the same time, newly formed gradients in stress, surface energy, fluid pressure, and/or temperature can generate differences in chemical potential. These gradients drive mineral dissolution, transport in solution, and subsequent precipitation, forming cements around the asperity contacts (*51*, *52*). Such cementation has important implications for fault mechanics. It contributes to fault strength recovery—or healing—because the precipitated minerals have intrinsic strength and promote increased contact area over time (*53*). This form of healing is distinct from frictional healing, which is often invoked to explain restrengthening in the seismogenic zone and in some shallow SSEs (*54*). In this model, grain angularity and high curvature are reintroduced during each SSE through cataclastic deformation and fracture of previously cemented contacts, effectively resetting the microstructure and allowing the healing cycle to repeat.

Fault strength is described by the Mohr-Coulomb criterion

$$\tau = c + \mu(\sigma - p) \tag{1}$$

The shear strength of the fault τ includes contributions from cohesion c, defined as the shear strength at zero normal stress, and frictional strength, which is a function of the coefficient of friction μ, the normal stress σ, and the pore fluid pressure p. Although the growth rates of mineral cements depend on pressure, temperature, and fluid composition, the resulting cementation can contribute to fault strength even in the absence of normal stress and is commonly quantified using the cohesion term c in Eq. 1. This definition of cohesion reflects shear resistance at zero effective normal stress and does not necessarily imply that cohesion is independent of all stress history. Rather, c is used here to capture bonding strength that may persist as a result of cementation even when normal stress is low or zero, as distinct from frictional strength that scales directly with effective normal stress. Although cementation is widely acknowledged to be an important process affecting faults, with some exceptions [e.g., (*55*)], cohesion is not regularly incorporated into numerical models of fault slip such as earthquake cycle simulations because the experimental data are limited, and the resulting strength is not well constrained (*56*). This may be a good assumption on shallower faults given that the effective normal stress, $\sigma - p$, is likely large, making frictional strength the dominant term in Eq. 1, and because temperatures are lower, so cementation reactions are slower. Significantly elevated pore fluid pressures, like those inferred in SSE environs, diminish the contribution of friction to the overall fault strength; hence, cohesion may become important or even dominant because it provides a source of strength at vanishingly small effective normal stress (*53*, *57*).

RESULTS

Simulating fault healing under SSE conditions with petrologic experiments

Whether rapid cementation and resulting cohesion play a role in generating the secondary fronts discussed above requires determining both the rates of cementation and the cohesive strength of cement under deep SSE conditions in Cascadia. To explore fault healing under these conditions, we perform a suite of petrologic experiments designed to simulate the fault zone immediately after an SSE has occurred. These conditions are characterized by pore fluids at nearly lithostatic pressures within a matrix of rock with newly formed surfaces owing to the breaking of contacts and, potentially, comminution (*58*) as well as heterogeneous stress distributions at the grain scale that begin to reequilibrate. For our experiments, we evaluate the cementation of crushed and sieved (104 to 125 μm) quartz containing saline or deionized pore water, which serves as simplified analogs for silicate rock and subduction zone fluid, respectively. To produce cementation, the quartz and fluid are loaded into a silver capsule, welded shut, heated, and pressurized to SSE conditions (i.e., temperatures of ~500°C and confining pressures of ~1 GPa) for time periods between 0 and 24 hours. After each experiment, we evaluate the processes and effects of cementation using scanning electron microscope (SEM) imaging and measuring the seismic velocities of the run products, respectively (see Materials and Methods for more details).

Although pore pressure is not directly measured in these experiments, we assume that sealed pore fluids reach nearly lithostatic pressure because of porosity collapse during compaction. Quartz aggregates at these temperatures and water contents are expected to compact through grain crushing and crystal plasticity, reducing porosity until internal fluid pressure equilibrates with the confining pressure. This assumption is consistent with prior high-pressure deformation studies of water-rich quartz systems, which either estimate nearly lithostatic conditions from final porosity [e.g., (*59*, *60*)] or explicitly adopt this assumption for interpreting mechanical behavior [e.g., (*61*)].

The starting crushed quartz is characterized by angular edges and conchoidal fracture (Fig. 3, A and B). After 6 hours at elevated pressure and temperature, quartz fragments have rounded grain edges, interlocked crystals, protofacets, and growth of small grains that were not present in the starting material (see Fig. 3, C and D, versus Fig. 3B) and are diagnostic of dissolution and precipitation processes (Fig. 3, C and D). The white ellipses in Fig. 3D show examples of healed grain boundary contacts. In some cases, these contacts also contain fluid inclusions, which are evidence of mineral precipitation along grain contacts. At longer timescales (24 hours), dissolution and precipitation of quartz are even more apparent, with well-developed facets and many fully healed grain boundaries pervading the sample (Fig. 3, E and F).

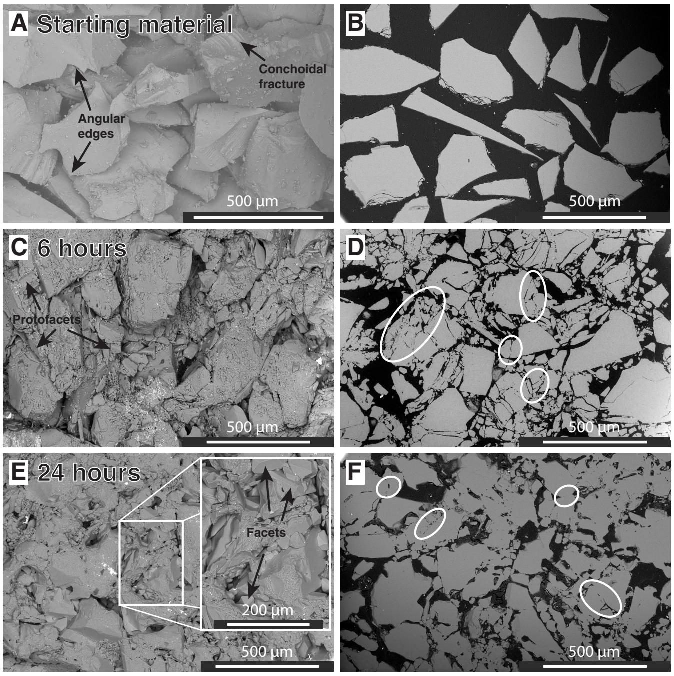

Fig. 3. 3D and 2D SEM images of starting, 6-hour, and 24-hour experiments. Each panel has a 500-μm scale bar. (**A**) SEM image of the quartz starting material. (**B**) SEM image of a polished grain mount of quartz starting material. The black background represents epoxy. (**C** and **D**) SEM images of the 6-hour experiment. (**E** and **F**) SEM images of the 24-hour experiment. White ellipses in (D) and (F) highlight a few (of many) examples of healed grain contacts and, in some cases, fluid inclusions. The inset in (F) shows an enlarged region of the background image with clear facets.

On natural faults, laboratory-derived estimates of quartz precipitation rates are often used to characterize timescales of fault healing [e.g., (*52*, *62*, *63*)]. We do not apply these frameworks here because the initial fluids in our experiments do not contain dissolved silica and are not supersaturated with respect to quartz, suggesting that bulk chemical supersaturation is not driving the sample evolution shown in Fig. 3. Instead, the dissolution-precipitation processes we observe in our experiments are likely driven by gradients in surface energy or pressure. For example, Beeler and Hickman (*51*) conducted a set of contact overgrowth experiments where they documented dissolution in high-energy, low-curvature pore walls, diffusive transport through the fluid, and precipitation in the low-energy, high-curvature contact periphery, resulting in cementation and overall contact growth. Alternatively, gradients in pressure can cause dissolution at grain-to-grain contacts, diffusive transfer to the pore space, and precipitation at the grain surface [e.g., (*64*)]. Kinetic rate laws do not fully capture either of these processes.

Measuring the cohesive strength as a function of healing time is an experimental challenge owing to the small sample sizes and capsule jacket. We are actively developing new experimental capabilities to make such measurements. An alternative way to obtain estimates of cohesive strength is by measuring wave speeds of each experimental capsule. Increases in the strength of grain-to-grain contacts and the closure of microcracks—whether through the dissolution-precipitation processes evident in Fig. 3 or grain bonding more generally—stiffen the rock and increase its elastic moduli. Because seismic wave speeds depend directly on these moduli, such microstructural changes can be indirectly linked to changes in seismic velocity. *P*-wave travel times are recorded using a compressive wave transducer, and sample lengths are measured using a caliper-style micrometer (see Materials and Methods). There is a clear increase in wave speed as a function of experiment duration (Fig. 4A). To evaluate the strength reflected by this increase in wave velocity, we apply two different empirical velocity-strength relationships to convert the measured wave speeds to estimates of change in cohesion, assuming an internal angle of friction of 35° (see Methods and Materials) (*65*, *66*). The results, shown in Fig. 4B, corroborate the SEM images and demonstrate that significant healing can occur on tidal timescales. For example, the McNally (*65*) and Fjær *et al.* (*66*) conversions predict 2.59 and 0.97 MPa of cohesion for the 12-hourexperiment, respectively. We note here that the estimates presented in Fig. 4B should be regarded as first-order estimates, as the McNally (*65*) and Fjær *et al.* (*66*) conversions were calibrated using sandstones and may not be applicable to our experimental samples. Nevertheless, the timescales and amplitudes reported in Fig. 4B are similar to values reported in other experimental studies that have attempted to measure timescales and amplitudes of cohesive strengthening or hydrothermal permeability reduction (*67*–*73*).

We note that the experiments shown in Fig. 3 were conducted with a saline solution matching seawater composition, while those in Fig. 4 used deionized water. Saline fluids can enhance the kinetics of interface-controlled healing processes, so the cohesion increases reported in Fig. 4 may represent a lower bound on healing rates. We initially used saline water to simulate subduction zone fluid compositions but switched to deionized water to simplify interpretation and eliminate salt crystallization observed in early SEM images. Future experiments will systematically explore the role of fluid composition in healing kinetics.

Cohesion on natural faults

To extend these experimental results to natural faults, we define c from Eq. 1 as

$$c = \tau_c A_c(t) \tag{2}$$

where τ_c is the cohesive strength of the cemented material, and $A_c(t)$ is the fractional contact area of the cement as a function of time. Our experiments provide a minimum bound on τ_c between 1.45 and 3.97 MPa from the McNally (*65*) and Fjær *et al.* (*66*) conversions, respectively. If we take a representative value of τ_c of 2 MPa and combine this with fractional contact area growth rates parameterized by Beeler (*53*), we find that cementation can contribute 20, 26, and 35 kPa of cohesion to the overall fault strength after 6, 12, and 24 hours, respectively. These fault strengths can easily accommodate stress drops more than the median 8 kPa estimated by Hawthorne *et al.* (*19*). In addition, Royer *et al.* (*13*) estimate an effective normal stress (i.e., $\sigma - p$) of 0.2 MPa. When combined with estimated friction coefficient of <=0.1 from Houston (*23*), the contribution of friction to the overall fault strength is <=20 kPa, similar in magnitude to our estimates of cohesion.

DISCUSSION

While cementation processes likely generate cohesion on all faults, the high temperatures, high pressures, and pervasiveness of fluids at nearly lithostatic pressure thought to exist in the environment of deep SSEs in Cascadia promote rapid cementation. Furthermore, the nearly lithostatic pore fluid pressures diminish the role of frictional strength (see Eq. 1), making cohesion an important, potentially dominant component of fault strength. As such, secondary slip fronts may reflect the interplay between fault healing and tidal loading, occurring when the fault has regained enough strength to accommodate an additional stress drop and the tides reload the fault beyond this threshold. In addition to the representative temperature, pressure, and pore fluid pressures we explore here, grain

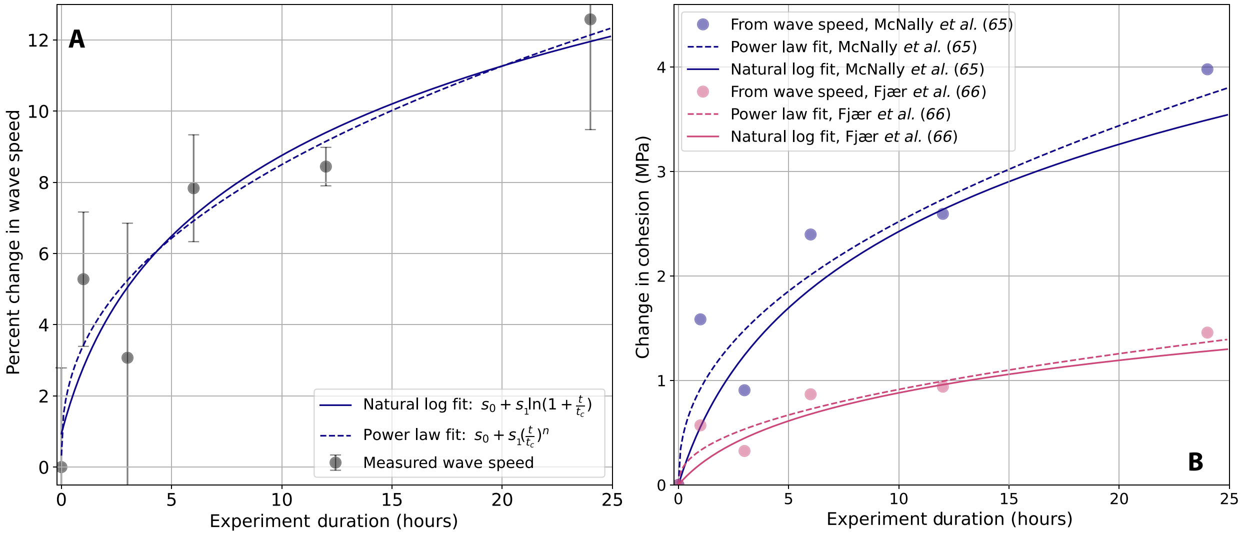

Fig. 4. Wave speed and cohesion versus duration. (**A**) Fractional change in measured wave speeds relative to 0-hour experiment as a function of experiment duration with best-fitting power law and natural log functional forms. The best-fitting natural log fit has parameters $s_0 = 3001.8$ m/s, $s_1 = 121.1$ m/s, and $t_c = 1.72$ hours. The best-fitting power law fit has parameters $s_0 = 2983.5$ m/s, $s_1 = 165.6$ m/s, $t_c = 4.00$ hours, and $n = 0.42$. (**B**) Change in cohesion as a function of experiment duration. The change in cohesion is computed from the measured wave speeds using the empirical relationships by McNally (*65*) and Fjær *et al.* (*66*).

size, grain composition, fluid composition, and fluid/rock ratios likely also significantly affect cementation rates and strengths.

Rapid and significant cohesive restrengthening addresses several challenges posed by friction-based models of deep SSEs. First, although frictional slip can produce slow slip [e.g., (*33*, *74*, *75*)], experimental evidence shows that many fault materials become rate-strengthening at the high temperatures typical of deep SSE conditions. This makes them incapable of sustaining unstable slip (*75*–*79*). Cohesion, in contrast, enables stick-slip behavior even in rate-strengthening materials. Second, while most SSE models emphasize large-scale creep, SSEs are frequently accompanied by small-scale radiative failures such as tremor and LFEs. The low effective stresses inferred at these depths make it difficult to explain how such seismic events nucleate, given that the critical nucleation dimension is inversely related to effective stress (*80*). Cohesion helps resolve this issue by allowing both distributed creep and localized seismic failure (*53*). Third, mechanisms often invoked to limit slip speed in SSE models—such as dilatancy hardening (*81*), transitions from velocity-weakening to velocity-strengthening friction (*42*), or frictional-viscous mixtures (*82*, *83*)—can inhibit the rapid slip needed to generate tremor and LFEs. This is problematic because LFEs and tremor appear to slip much faster than the SSEs they accompany [e.g., (*6*)]. Fourth, adding cohesion increases the overall fault strength and allows for larger stress drops, which may enable secondary fronts to propagate at speeds consistent with those observed (*42*). Last, although this study emphasizes cohesion as a time-dependent strengthening mechanism, we note that variations in fault geometry may also contribute to shear resistance under near-zero effective stress conditions. We view cohesion and fault zone heterogeneity as complementary mechanisms that can together help explain the observed complexity and variability in slow slip behavior.

While this work specifically focuses on SSEs, cohesion could also be an important component of fault strength within the seismogenic zone. Experiments that explore the role of temperature in asperity contact overgrowths find that the volumetric growth rates change by a factor of 16 per 100°C (*42*). Using these constraints, the asperity contact growth that takes place at 500°C during the typical 1-year recurrence interval of northern Cascadia SSEs would take 70 years at 350°C (the base of the seismogenic zone). Seventy years is far less than the average 500-year recurrence interval of great megathrust earthquakes in Cascadia, so the temperature difference between the seismogenic zone and deeper SSEs does not prohibit significant strengthening in the seismogenic zone. Additional support for this idea comes from hydrogeologic observations at shallow depths, which also suggest rapid fault healing over timescales of days following large earthquakes, perhaps driven by similar mechanisms [e.g., (*84*, *85*)]. However, the elevated effective stresses thought to be present may limit the contribution of cohesion to the overall fault strength. Nevertheless, the observations and experimental results we present here provide strong motivation for reconsidering and better characterizing the role of cementation and resulting cohesion in SSEs and earthquakes in general.

MATERIALS AND METHODS

Motivation for experimental setup

While quartz aggregate itself is not a likely analog for slow earthquakes in nature, our experimental design was intentionally simplified to isolate the fundamental mechanisms of fluid-assisted healing following SSEs. Specifically, we used an aggregate of angular quartz grains rather than more compositionally complex natural rock assemblages. While natural rocks may more closely approximate subduction zone fault materials (e.g., talc-bearing blueschists or mélanges), they introduce substantial experimental challenges that hinder equilibration and interpretation.

Quartz was chosen as the experimental phase for two main reasons. First, in natural settings, fluid and mineral assemblages are likely in chemical equilibrium before slow slip. Reproducing this condition in the lab is critical. However, achieving chemical equilibrium in multiphase rocks at 500°C would require the simultaneous reaction of multiple minerals governed by poorly constrained kinetic parameters. Preequilibrating such assemblages would likely require static runs of weeks to months and introduce an additional uncertainty. Second, quartz is a single phase with well-documented dissolution-precipitation kinetics. Data from Rimstidt and Barnes (*62*) allow for quantitative estimation of chemical equilibration times. At 500°C, equilibration of 100-μm grains is expected to occur in ~10 min, providing the desired initial condition of fluid-rock equilibrium.

By using a quartz aggregate, we were able to achieve chemical and microstructural equilibration before deformation and thus simulate disequilibrium driven by mechanical effects such as stress gradients and curvature. This setup enables a clean investigation of grain-scale healing processes, particularly cementation and cohesion development, under controlled and interpretable conditions.

Piston-cylinder experiments

Our piston-cylinder experiments are split into two categories: small-capsule experiments for imaging and characterization and large-capsule experiments for wave speed measurements. Small-capsule experiments were run using a $^{1}/_{2}$-inch (1.27 cm)–diameter assembly with MgO-CaF$_2$ crushable materials (fig. S1). Silver or silver-palladium capsules (10-mm length, 3.0-mm outer diameter, and 0.15-mm wall thickness) were annealed at 900°C, then crimped, and welded at one end before loading with ~30 to 40 mg of crushed synthetic quartz (180 to 350 μm, dry-sieved) and 10 μl of "subduction fluid" ($[Na^+] = 400$ mM; $[Ca^{2+}] = 30$ mM; $[K^+] = 15$ mM; $[Cl^-] = 460$ mM), which is similar to seawater without Mg^{2+} [compare (*86*)]. After loading, the capsules were crimped and welded, weighed, stored in an oven at >110°C, and reweighed to ensure that they retained fluid. Large-capsule experiments were run using a $^{3}/_{4}$-inch (1.905 cm)–diameter assembly with MgO-NaCl crushable materials (fig. S1). Silver capsules (6.4-mm outer diameter and 0.7-mm wall thickness) and garbage can-shaped lids (0.5-mm thickness) were annealed at 900°C. For each experiment, the lid was welded at one end before the capsule was loaded with ~175 mg of crushed quartz (104 to 125 μm, wet-sieved) and 50 μl of deionized water. After loading, a lid was welded to the open end, and the capsule was weighed, stored in an oven at >110°C, and reweighed to ensure that it retained fluid.

In the piston-cylinder apparatus, sample assemblies were cold pressurized to about 1 GPa and then heated to 500°C at a ramp rate of ~150°C/min. During the ramp, the sample pressure decreased to nearly 1 GPa and was adjusted manually, as necessary, during the run. The hydraulic oil pressure applied to the sample was measured with a Heise-Bourdon tube pressure gauge (serial no. CM107-526) and converted to the pressure exerted on the sample without applying any friction corrections. The temperature was controlled to within 5°C using type C thermocouples ($W_{25}Re$-W_6Re) and Eurotherm proportional-integral-derivative controllers. Each experiment was quenched within seconds by shutting off power. After each small-capsule experiment, the run products were retrieved by cutting capsules open using a Bico diamond wafer saw. Upon inspection, we found no clear evidence for textural changes arising from the quench (e.g., cracking or precipitation of SiO_2 quench spheres) (*87*), which we attribute to the low solubility of SiO_2 at 500°C [~8 ppm (parts per million)] (*88*).

The small- and large-capsule experiments differ in capsule size, grain size distribution, and pore fluid composition. These differences reflect the staged development of the project and were made to improve imaging quality, simplify interpretation, and reduce experimental uncertainty. The small-capsule experiments—used for SEM imaging—were conducted using a wider grain size distribution (180 to 350 μm, dry-sieved) and a synthetic brine ("subduction fluid") that approximates chloride concentrations expected in subduction zone fluids. These conditions were chosen at the outset to maximize the chances of observing any microstructural changes on short timescales.

The promising results from these early experiments motivated the development of large-capsule experiments to allow ultrasonic wave speed measurements. In scaling up, we made three changes: (i) We switched to deionized water to avoid salt precipitation artifacts in recovered samples; (ii) we narrowed the grain size to 104 to 125 μm and removed fines by wet sieving to reduce complexity in interpretation; and (iii) we increased the sample size to enable nondestructive wave speed measurements. Each of these changes was intended to simplify analysis or improve data quality. Notably, the changes to fluid composition and grain size are likely to result in slower healing kinetics, making the velocity-derived estimates of cohesion in the large-capsule experiments conservative. Although the two sets of experiments differ in design, the agreement between independent indicators—microstructure and wave speed—strengthens the conclusion that rapid cohesive healing occurs on timescales of hours under subduction-relevant *P*-*T* conditions.

SEM imaging

Crystals were imaged and analyzed at the Center for Advanced Materials Characterization in Oregon at the University of Oregon on a Thermo Fisher Scientific Apreo 2 S SEM at 10 or 15 keV with a beam current of 1.6 nA. All images presented herein were obtained using a concentric backscattered detector in low-vacuum mode. The "three-dimensional" (3D) images are taken, looking into the capsule without any sample preparation. The "2D" images are of polished sections that are mounted in epoxy.

Wave speed measurements

The ends of the recovered samples from large-capsule experiments were ground flat with 240-grit silica carbide on a glass plate. The removed material was primarily remnant confining media adhered to the silver jackets as well as a small amount of the peripheral capsule welds. The resulting ground end interfaces consist of an outer rim of silver corresponding to the welded closure of the capsule and, interior to the rim, a circular region of confining media (fig. S2). The sample length and travel times reported are measurements across the sample and small amounts of silver jacket and confining media at each of the ends. While approximately flat, the two sample ends are typically not exactly parallel.

The sample lengths were measured with a spring-loaded caliper-style micrometer with 0.00005″ (1.27 μm) precision. Four successive length measurements were made on each sample following ~70° rotations about its axis. The sample length measurements have a fractional variability of less than 0.4%.

Single-period, 5-V peak-to-peak amplitude, 1-MHz frequency sine waves were sent every 0.1 s from one sample end using a $^1/_2$″ active diameter Panametrics V103 compressive wave transducer. A second identical transducer records the received wave at the other sample end (fig. S3). The sent waveform represents a positive voltage pulse to the transmitting transducer, which produces an outward deflection (compression), while the wave arriving at the receiving transducer causes an inward deflection (also compression), resulting in an output voltage with an opposite sign. The transducers were coupled to the sample ends using a highly viscous ultrasonic couplant (Echo Ultrasonics Shear Wave). The received waves are amplified 1000× (60 dB) using a Panametrics model 5800 pulser/receiver/amplifier. Both the sent and received waveforms were passively monitored with an oscilloscope and recorded at 100 MHz by a National Instruments NI PXIe-5122 data acquisition scope with a 14-bit digitizer. One thousand sent and received waveforms, corresponding to 100 s of measurement time, were recorded. The sample was then rotated about its axis by ~70°, and the above procedure was repeated. There were three rotations; thus, reported travel times are from four measurements on each sample.

Because our experimental samples are small relative to the ultrasonic wavelength and the active diameter of the transducers, we evaluated the potential impact of sample size on wave speed accuracy. The sample length-to-wavelength ratios in our experiments approach or fall below typical thresholds recommended in American Society for Testing and Materials/American National Standards Institute standards (e.g., D2845), raising a concern that the transducer-sample size mismatch might introduce measurement artifacts. Although we initially considered using smaller-diameter transducers (~$^1/_4$″) to better match sample dimensions, this introduced alignment difficulties and poor acoustic coupling that ultimately reduced measurement reliability.

To empirically assess the accuracy of our setup, we conducted tests using silica glass rods with known, homogeneous elastic properties. These rods had diameters of 13, 6.4, and 3 mm (~0.5″, 0.25″, and 0.12″, respectively) and lengths comparable to those of the experimental samples (~0.3″). The wave speeds measured in these rods were consistent with 1%, with uncertainties of 0.4 to 2%, despite the rods being from different manufacturing batches. The 6.4- and 13-mm diameters bracket the range of both our sample diameters (0.26″ to 0.29″) and the active diameter of the transducers. The close agreement between their measured wave speeds confirms that the sensor-to-sample diameter mismatch does not significantly bias our results. The received waveforms in smaller-diameter rods (6.4 and 3 mm) exhibited greater complexity, like the experimental samples, while the larger 13-mm rods produced simpler waveforms. Despite increased complexity, the first arrivals remained sharp and repeatable, even in the 3-mm-diameter rods, where the length-to-wavelength ratio was as low as ~1.25. These tests demonstrate that meaningful arrival times can be extracted reliably under such conditions, even though they fall outside American Society for Testing and Materials–specified geometries.

Additional care was taken throughout to ensure accurate wave speed determination, including verification of signal polarity, avoidance of capsule-related precursors, identification of sharp initial peaks, and careful transducer placement to minimize side reflections. These precautions, along with our validation tests, support the conclusion that the small sample dimensions did not compromise our ability to accurately determine *P*-wave onset times and velocities.

Across the experimental samples, the received waveforms are more complex overall, but the initial arrivals remain well defined. Figure S4 shows a representative example from the 3-hour experiment. The received wave onset (red) includes a distinct downward deflection followed by a larger upward deflection—features consistent with the transmitted waveform (blue) and suitable for accurate arrival time picking. Complexity in the later wave train, including rounded peaks and prolonged ringing, likely results from internal reflections within the silver capsule or off the sample's lateral boundaries. Despite these later-arriving complexities, the sharpness and coherence of the initial motion support its use in wave speed determination. Complexity beyond the onset is not used in travel time analysis and does not affect the primary conclusions.

The travel time was measured on each set of 1000 records, which were cross-correlated and stacked. The reported travel time is the time difference between the first recorded points in the monotonic onset of the sent and received stacked records that exceeds the background noise. The travel times have a fractional variability of <3.5%. The reported variability of the wave speed is the sum of the length and travel time variability measurements. Sample lengths, travel times, wave speed estimates, and their uncertainties are reported in table S1. Dataset S1 contains the sent and received waveform stacks for each experiment.

Cohesion estimates

We use two empirical velocity-strength relationships to convert the wave speed measurements presented in Fig. 4 and table S1 to unconfined strength (UCS). The first equation that comes from Fjær *et al.* (*66*) is

$$\mathrm{UCS} = 1.4138 * 10^{7}\ \Delta t^{-3} \tag{3}$$

where Δt is the travel time in microseconds per foot, and UCS is in megapascals. The second equation, from McNally (*65*), is

$$\mathrm{UCS} = 1200 * \exp\left(-0.036 * \Delta t\right) \tag{4}$$

We then convert UCS to cohesion, assuming an internal angle of friction of 35° using

$$c = \mathrm{UCS} * \left[1 - \sin(35 * \pi/180)\right] / \left[2 * \cos(35 * \pi/180)\right] \tag{5}$$

where c is cohesion in megapascals. We note that a larger assumed friction angle leads to lower c for a given UCS. Given that the transducer measurements undoubtedly are influenced by the silver capsule material, we report the change in cohesion, i.e., the calculated cohesion less the cohesion of the 0-hour duration experiment instead of the absolute values.

Supplementary Materials

The PDF file includes:

Figs. S1 to S4
Tables S1 and S2
Legend for dataset S1

Other Supplementary Material for this manuscript includes the following:

Dataset S1

REFERENCES AND NOTES

1. R. Bürgmann, The geophysics, geology and mechanics of slow fault slip. *Earth Planet. Sci. Lett.* **495**, 112–134 (2018).
2. W. M. Behr, R. Bürgmann, What's down there? The structures, materials and environment of deep-seated slow slip and tremor. *Philos. Trans. R. Soc. A* **379**, 20200218 (2021).
3. A. G. Wech, K. C. Creager, Automated detection and location of Cascadia tremor. *Geophys. Res. Lett.* **35**, L20302 (2008).
4. G. Rogers, H. Dragert, Episodic tremor and slip on the Cascadia subduction zone: The chatter of silent slip. *Science* **300**, 1942–1943 (2003).
5. D. R. Shelly, G. C. Beroza, S. Ide, Non-volcanic tremor and low-frequency earthquake swarms. *Nature* **446**, 305–307 (2007).
6. A. M. Thomas, G. C. Beroza, D. R. Shelly, Constraints on the source parameters of low-frequency earthquakes on the San Andreas Fault. *Geophys. Res. Lett.* **43**, 1464–1471 (2016).
7. M. G. Bostock, A. M. Thomas, G. Savard, L. Chuang, A. M. Rubin, Magnitudes and moment-duration scaling of low-frequency earthquakes beneath southern Vancouver Island. *J. Geophys. Res. Solid Earth* **120**, 6329–6350 (2015).
8. A. M. Thomas, N. M. Beeler, Q. Bletery, R. Bürgmann, D. R. Shelly, Using low-frequency earthquake families on the San Andreas Fault as deep creepmeters. *J. Geophys. Res. Solid Earth* **123**, 457–475 (2018).
9. A. Ghosh, J. E. Vidale, J. R. Sweet, K. C. Creager, A. G. Wech, H. Houston, E. E. Brodsky, Rapid, continuous streaking of tremor in Cascadia. *Geochem. Geophys. Geosyst.* **11**, Q12010 (2010).
10. H. Houston, B. G. Delbridge, A. G. Wech, K. C. Creager, Rapid tremor reversals in Cascadia generated by a weakened plate interface. *Nat. Geosci.* **4**, 404–409 (2011).
11. A. M. Rubin, J. G. Armbruster, Imaging slow slip fronts in Cascadia with high precision cross-station tremor locations. *Geochem. Geophys. Geosyst.* **14**, 5371–5392 (2013).
12. Y. Peng, A. M. Rubin, M. G. Bostock, J. G. Armbruster, High-resolution imaging of rapid tremor migrations beneath southern Vancouver Island using cross-station cross correlations. *J. Geophys. Res. Solid Earth* **120**, 4317–4332 (2015).
13. A. A. Royer, A. M. Thomas, M. G. Bostock, Tidal modulation and triggering of low-frequency earthquakes in northern Cascadia. *J. Geophys. Res. Solid Earth* **120**, 384–405 (2015).
14. Q. Bletery, A. M. Thomas, J. C. Hawthorne, R. M. Skarbek, A. W. Rempel, R. D. Krogstad, Characteristics of secondary slip fronts associated with slow earthquakes in Cascadia. *Earth Planet. Sci. Lett.* **463**, 212–220 (2017).
15. K. Obara, T. Matsuzawa, S. Tanaka, T. Maeda, Depth-dependent mode of tremor migration beneath Kii Peninsula, Nankai subduction zone. *Geophys. Res. Lett.* **39**, L10308 (2012).
16. Y. Peng, A. M. Rubin, Simulating short-term evolution of slow slip influenced by fault heterogeneities and tides. *Geophys. Res. Lett.* **45**, 10269–10278 (2018).
17. Y. Peng, A. M. Rubin, Intermittent tremor migrations beneath Guerrero, Mexico, and implications for fault healing within the slow slip zone. *Geophys. Res. Lett.* **44**, 760–770 (2017).
18. A. Inbal, A. M. Thomas, T. Newton, R. Bürgmann, Complex migration of tremor near Cholame, CA, resolved by seismic array analysis. *J. Geophys. Res. Solid Earth* **126**, e2021JB022174 (2021).
19. J. C. Hawthorne, M. G. Bostock, A. A. Royer, A. M. Thomas, Variations in slow slip moment rate associated with rapid tremor reversals in Cascadia. *Geochem. Geophys. Geosyst.* **17**, 4899–4919 (2016).
20. J. L. Rubinstein, M. La Rocca, J. E. Vidale, K. C. Creager, A. G. Wech, Tidal modulation of nonvolcanic tremor. *Science* **319**, 186–189 (2008).
21. A. M. Thomas, R. M. Nadeau, R. Bürgmann, Tremor-tide correlations and near-lithostatic pore pressure on the deep San Andreas Fault. *Nature* **462**, 1048–1051 (2009).
22. A. M. Thomas, R. Bürgmann, D. R. Shelly, N. M. Beeler, M. L. Rudolph, Tidal triggering of low-frequency earthquakes near Parkfield, California: Implications for fault mechanics within the brittle-ductile transition. *J. Geophys. Res. Solid Earth* **117**, B05301 (2012).
23. H. Houston, Low friction and fault weakening revealed by rising sensitivity of tremor to tidal stress. *Nat. Geosci.* **8**, 409–415 (2015).
24. S. Yabe, Y. Tanaka, H. Houston, S. Ide, Tidal sensitivity of tectonic tremors in Nankai and Cascadia subduction zones. *J. Geophys. Res. Solid Earth* **120**, 7587–7605 (2015).
25. J. C. Hawthorne, A. M. Rubin, Tidal modulation of slow slip in Cascadia. *J. Geophys. Res. Solid Earth* **115**, B09406 (2010).
26. T. W. Thomas, J. E. Vidale, H. Houston, K. C. Creager, J. R. Sweet, A. Ghosh, Evidence for tidal triggering of high-amplitude rapid tremor reversals and tremor streaks in northern Cascadia. *Geophys. Res. Lett.* **40**, 4254–4259 (2013).
27. P. Audet, M. G. Bostock, N. I. Christensen, S. M. Peacock, Seismic evidence for overpressured subducted oceanic crust and megathrust fault sealing. *Nature* **457**, 76–78 (2009).
28. S. M. Peacock, N. I. Christensen, M. G. Bostock, P. Audet, High pore pressures and porosity at 35 km depth in the Cascadia subduction zone. *Geology* **39**, 471–474 (2011).

29. P. Audet, R. Bürgmann, Possible control of subduction zone slow-earthquake periodicity by silica enrichment. *Nature* **510**, 389–392 (2014).
30. J. R. Delph, A. Levander, F. Niu, Fluid controls on the heterogeneous seismic characteristics of the Cascadia margin. *Geophys. Res. Lett.* **45**, 11021–11029 (2018).
31. A. J. Calvert, M. G. Bostock, G. Savard, M. J. Unsworth, Cascadia low frequency earthquakes at the base of an overpressured subduction shear zone. *Nat. Commun.* **11**, 3874 (2020).
32. J. R. Delph, A. M. Thomas, A. Levander, Subcretionary tectonics: Linking variability in the expression of subduction along the Cascadia forearc. *Earth Planet. Sci. Lett.* **556**, 116724 (2021).
33. N. M. Beeler, A. Thomas, R. Bürgmann, D. Shelly, Inferring fault rheology from low-frequency earthquakes on the San Andreas. *J. Geophys. Res. Solid Earth* **118**, 5976–5990 (2013).
34. K. Ujiie, H. Saishu, Å. Fagereng, N. Nishiyama, M. Otsubo, H. Masuyama, H. Kagi, An explanation of episodic tremor and slow slip constrained by crack-seal veins and viscous shear in subduction mélange. *Geophys. Res. Lett.* **45**, 5371–5379 (2018).
35. J. D. Kirkpatrick, Å. Fagereng, D. R. Shelly, Geological constraints on the mechanisms of slow earthquakes. *Nat. Rev. Earth Environ.* **2**, 285–301 (2021).
36. S. M. Peacock, Thermal and metamorphic environment of subduction zone episodic tremor and slip. *J. Geophys. Res. Solid Earth* **114**, B00A07 (2009).
37. C. B. Condit, V. E. Guevara, J. R. Delph, M. E. French, Slab dehydration in warm subduction zones at depths of episodic slip and tremor. *Earth Planet. Sci. Lett.* **552**, 116601 (2020).
38. M. McLellan, P. Audet, J. C. Rosas, C. Currie, Margin-wide variations in slab dehydration in Cascadia and their relationship to slow slip. *Lithos* **434-435**, 106912 (2022).
39. W. F. Brace, J. D. Byerlee, Stick-slip as a mechanism for earthquakes. *Science* **153**, 990–992 (1966).
40. V. M. Cruz-Atienza, C. Villafuerte, H. S. Bhat, Rapid tremor migration and pore-pressure waves in subduction zones. *Nat. Commun.* **9**, 2900 (2018).
41. J. H. Dieterich, B. D. Kilgore, Direct observation of frictional contacts: New insights for state-dependent properties. *Pure Appl. Geophys.* **143**, 283–302 (1994).
42. J. C. Hawthorne, A. M. Rubin, Tidal modulation and back-propagating fronts in slow slip events simulated with a velocity-weakening to velocity-strengthening friction law. *J. Geophys. Res. Solid Earth* **118**, 1216–1239 (2013).
43. Y. Luo, Z. Liu, Fault zone heterogeneities explain depth-dependent pattern and evolution of slow earthquakes in Cascadia. *Nat. Commun.* **12**, 1959 (2021).
44. D. M. Fisher, S. L. Brantley, Models of quartz overgrowth and vein formation: Deformation and episodic fluid flow in an ancient subduction zone. *J. Geophys. Res.* **97**, 20043–20061 (1992).
45. D. M. Fisher, S. L. Brantley, The role of silica redistribution in the evolution of slip instabilities along subduction interfaces: Constraints from the Kodiak accretionary complex, Alaska. *J. Struct. Geol.* **69**, 395–414 (2014).
46. Å. Fagereng, J. F. A. Diener, S. Ellis, F. Remitti, "Fluid-related deformation processes at the up- and downdip limits of the subduction thrust seismogenic zone: What do the rocks tell us?" in *Geology and Tectonics of Subduction Zones: A Tribute to Gaku Kimura*, T. Byrne, M. B. Underwood, D. M. Fisher, L. McNeill, D. Saffer, K. Ujiie, A. Yamaguchi, Eds. (Geological Society of America, 2018), chap. 12, vol. 534.
47. A. J. Kotowski, W. M. Behr, Length scales and types of heterogeneities along the deep subduction interface: Insights from exhumed rocks on Syros Island, Greece. *Geosphere* **15**, 1038–1065 (2019).
48. C. B. Condit, M. E. French, Geologic evidence of lithostatic pore fluid pressures at the base of the subduction seismogenic zone. *Geophys. Res. Lett.* **49**, e2022GL098862 (2022).
49. J. Muñoz-Montecinos, W. M. Behr, Transient permeability of a deep-seated subduction interface shear zone. *Geophys. Res. Lett.* **50**, e2023GL104244 (2023).
50. F. M. Chester, J. P. Evans, R. L. Biegel, Internal structure and weakening mechanisms of the San Andreas Fault. *J. Geophys. Res.* **98**, 771–786 (1993).
51. N. M. Beeler, S. H. Hickman, Direct measurement of asperity contact growth in quartz at hydrothermal conditions. *J. Geophys. Res. Solid Earth* **120**, 3599–3616 (2015).
52. R. T. Williams, Å. Fagereng, The role of quartz cementation in the seismic cycle: A critical review. *Rev. Geophys.* **60**, e2021RG000768 (2022).
53. N. M. Beeler, Brittle faulting at elevated temperature and vanishing effective stress. *J. Geophys. Res. Solid Earth* **127**, e2022JB024335 (2022).
54. S. Shreedharan, D. Saffer, L. M. Wallace, C. Williams, Ultralow frictional healing explains recurring slow slip events. *Science* **379**, 712–717 (2023).
55. J. N. Hooker, D. M. Fisher, How cementation and fluid flow influence slip behavior at the subduction interface. *Geology* **49**, 1074–1078 (2021).
56. S. Barbot, A rate-, state-, and temperature-dependent friction law with competing healing mechanisms. *J. Geophys. Res. Solid Earth* **127**, e2022JB025106 (2022).
57. M. P. A. Van Den Ende, A. R. Niemeijer, An investigation into the role of time-dependent cohesion in interseismic fault restrengthening. *Sci. Rep.* **9**, 9894 (2019).
58. K. Been, M. G. Jefferies, J. H. Hachey, The critical state of sands. *Géotechnique* **41**, 365–381 (1991).
59. G. C. Gleason, J. T. Tullis, A flow law for dislocation creep of quartz aggregates determined with the molten salt cell. *Tectonophysics* **247**, 1–23 (1995).
60. K. Okazaki, E. Burdette, G. Hirth, Rheology of the fluid oversaturated fault zones at the brittle-plastic transition. *J. Geophys. Res. Solid Earth* **126**, e2020JB020804 (2021).
61. T. E. Tullis, J. D. Weeks, J. T. Tullis, Frictional sliding of feldspar at high temperature and high pressure. *Geology* **24**, 1027–1030 (1996).
62. J. D. Rimstidt, H. L. Barnes, The kinetics of silica-water reactions. *Geochim. Cosmochim. Acta* **44**, 1683–1699 (1980).
63. R. H. Lander, S. E. Laubach, Insights into rates of fracture growth and sealing from a model for quartz cementation in fractured sandstones. *Geol. Soc. Am. Bull.* **127**, 516–538 (2015).
64. H. Yasuhara, C. Marone, D. Elsworth, Fault zone restrengthening and frictional healing: The role of pressure solution. *J. Geophys. Res. Solid Earth* **110**, B06310 (2005).
65. G. H. McNally, *Estimation of Coal Measures Rock Strength Using Sonic and Neutron Logs* (Elsevier, Amsterdam, 1987), vol. 24, pp. 381–395.
66. E. Fjær, R. M. Holt, P. Horsrud, A. M. Raaen, *Petroleum Related Rock Mechanics* (Elsevier, Amsterdam, ed. 2, 2008).
67. S. L. Brantley, B. Evans, S. H. Hickman, D. A. Crerar, Healing of microcracks in quartz: Implications for fluid flow. *Geology* **18**, 136–139 (1990).
68. D. E. Moore, D. A. Lockner, J. D. Byerlee, Reduction of permeability in granite at elevated temperatures. *Science* **265**, 1558–1561 (1994).
69. S. L. Karner, C. Marone, B. Evans, Laboratory study of fault healing and lithification in simulated fault gouge under hydrothermal conditions. *Tectonophysics* **277**, 41–55 (1997).
70. S. K. Muhuri, T. A. Dewers, T. E. Scott, Z. Reches, Interseismic fault strengthening and earthquake-slip instability: Friction or cohesion? *Geology* **31**, 881–884 (2003).
71. E. Tenthorey, S. F. Cox, H. F. Todd, Evolution of strength recovery and permeability during fluid-rock reaction in experimental fault zones. *Earth Planet. Sci. Lett.* **206**, 161–172 (2003).
72. E. Tenthorey, S. F. Cox, Cohesive strengthening of fault zones during the interseismic period: An experimental study. *J. Geophys. Res. Solid Earth* **111**, B09202 (2006).
73. S. B. Giger, E. Tenthorey, S. F. Cox, J. D. Fitz Gerald, Permeability evolution in quartz fault gouges under hydrothermal conditions. *J. Geophys. Res. Solid Earth* **112**, B07202 (2007).
74. G. Hirth, N. M. Beeler, The role of fluid pressure on frictional behavior at the base of the seismogenic zone. *Geology* **43**, 223–226 (2015).
75. M. Takahashi, S.-I. Uehara, K. Mizoguchi, I. Shimizu, K. Okazaki, K. Masuda, On the transient response of serpentine (antigorite) gouge to stepwise changes in slip velocity under high-temperature conditions. *J. Geophys. Res. Solid Earth* **116**, B10405 (2011).
76. M. L. Blanpied, D. A. Lockner, J. D. Byerlee, Frictional slip of granite at hydrothermal conditions. *J. Geophys. Res.* **100**, 13045–13064 (1995).
77. D. E. Moore, D. A. Lockner, Talc friction in the temperature range 25–400°C: Relevance for fault-zone weakening. *Tectonophysics* **449**, 120–132 (2008).
78. S. A. M. Den Hartog, C. J. Spiers, Influence of subduction zone conditions and gouge composition on frictional slip stability of megathrust faults. *Tectonophysics* **600**, 75–90 (2013).
79. A. S. Okamoto, B. A. Verberne, A. R. Niemeijer, M. Takahashi, I. Shimizu, T. Ueda, C. J. Spiers, Frictional properties of simulated chlorite gouge at hydrothermal conditions: Implications for subduction megathrusts. *J. Geophys. Res. Solid Earth* **124**, 4545–4565 (2019).
80. A. Ruina, Slip instability and state variable friction laws. *J. Geophys. Res.* **88**, 10359–10370 (1983).
81. P. Segall, A. M. Rubin, A. M. Bradley, J. R. Rice, Dilatant strengthening as a mechanism for slow slip events. *J. Geophys. Res. Solid Earth* **115**, B12305 (2010).
82. W. M. Behr, T. V. Gerya, C. Cannizzaro, R. Blass, Transient slow slip characteristics of frictional-viscous subduction megathrust shear zones. *AGU Adv.* **2**, e2021AV000416 (2021).
83. R. Ando, K. Ujiie, N. Nishiyama, Y. Mori, Depth-dependent slow earthquakes controlled by temperature dependence of brittle-ductile transitional rheology. *Geophys. Res. Lett.* **50**, e2022GL101388 (2023).
84. L. Xue, H.-B. Li, E. E. Brodsky, Z.-Q. Xu, Y. Kano, H. Wang, J. J. Mori, J.-L. Si, J.-L. Pei, W. Zhang, G. Yang, Z.-M. Sun, Y. Huang, Continuous permeability measurements record healing inside the Wenchuan earthquake fault zone. *Science* **340**, 1555–1559 (2013).
85. P. M. Fulton, E. E. Brodsky, In situ observations of earthquake-driven fluid pulses within the Japan Trench plate boundary fault zone. *Geology* **44**, 851–854 (2016).
86. C. E. Manning, The chemistry of subduction-zone fluids. *Earth Planet. Sci. Lett.* **223**, 1–16 (2004).
87. A. Antignano, C. E. Manning, Rutile solubility in H_2O, H_2O-SiO_2, and H_2O-$NaAlSi_3O_8$ fluids at 0.7–2.0 GPa and 700–1000°C: Implications for mobility of nominally insoluble elements. *Chem. Geol.* **255**, 283–293 (2008).
88. B. Mysen, Aqueous fluids as transport medium at high pressure and temperature: Ti^{4+} solubility, solution mechanisms, and fluid composition. *Chem. Geol.* **505**, 57–65 (2019).

Acknowledgments: We thank D. Moore, R. Bürgmann, D. Shelly, and the anonymous reviewers for suggestions that greatly improved the quality of the manuscript. Any use of trade, firm, or product names is for descriptive purposes only and does not imply endorsement by the US Government. **Funding:** This work was supported by National Science Foundation grants 1848302 (to A.M.T.), 2533457 (to A.M.T., J.M.W., and M.H.R.), and 2420572 (to M.E.F.). **Author contributions:** Conceptualization: A.M.T., J.M.W., N.M.B., and M.E.F. Formal analysis: A.M.T., J.M.W., N.M.B., and M.E.F. Funding acquisition: A.M.T. Investigation: A.M.T., J.M.W., N.M.B., M.E.F., W.M.B., and M.H.R. Methodology: A.M.T., J.M.W., N.M.B., and M.E.F. Project administration: A.M.T. Resources: A.M.T., J.M.W., and N.M.B. Supervision: A.M.T. Validation: A.M.T., J.M.W., N.M.B., and W.M.B. Visualization: A.M.T., J.M.W., and N.M.B. Writing—original draft: A.M.T., J.M.W., and N.M.B. Writing—review and editing: M.E.F., W.M.B., and M.H.R. **Competing interests:** The authors declare that they have no competing interests. **Data and materials availability:** LFE data are from Bostock *et al.* (*7*) and are available from the Slow Earthquake Database (www-solid.eps.s.u-tokyo.ac.jp/~sloweq/). Tremors are identified using the method described by Wech and Creager (*3*) and are available from the Pacific Northwest Seismic Network (www.pnsn.org/). Wave speed measurements are listed in the Supplementary Materials. All data needed to evaluate the conclusions in the paper are present in the paper and/or the Supplementary Materials.

Submitted 25 May 2025
Accepted 23 October 2025
Published 19 November 2025
10.1126/sciadv.adz2832